

Article

Magnetic Phase Diagram of the $Mn_xFe_{2-x}P_{1-y}Si_y$ System

Xinmin You , Michael Maschek, Niels Harmen H. van Dijk and Ekkes Brück *

Fundamental Aspects of Materials and Energy (FAME), Faculty of Applied Sciences, Delft University of Technology, Mekelweg 15, 2629 JB Delft, The Netherlands; x.you-1@tudelft.nl (X.Y.); M.Maschek@tudelft.nl (M.M.); n.h.vandijk@tudelft.nl (N.H.H.v.D.)

* Correspondence: e.h.bruck@tudelft.nl

Abstract: The phase diagram of the magnetocaloric $Mn_xFe_{2-x}P_{1-y}Si_y$ quaternary compounds was established by characterising the structure, thermal and magnetic properties in a wide range of compositions (for a Mn fraction of $0.3 \leq x < 2.0$ and a Si fraction of $0.33 \leq y \leq 0.60$). The highest ferromagnetic transition temperature ($Mn_{0.3}Fe_{1.7}P_{0.6}Si_{0.4}$, $T_C = 470$ K) is found for low Mn and high Si contents, while the lowest is found for low Fe and Si contents ($Mn_{1.7}Fe_{0.3}P_{0.6}Si_{0.4}$, $T_C = 65$ K) in the $Mn_xFe_{2-x}P_{1-y}Si_y$ phase diagram. The largest hysteresis (91 K) was observed for a metal ratio close to Fe:Mn = 1:1 (corresponding to $x = 0.9$, $y = 0.33$). Both Mn-rich with high Si and Fe-rich samples with low Si concentration were found to show low hysteresis (≤ 2 K). These compositions with a low hysteresis form promising candidate materials for thermomagnetic applications.

Keywords: magnetocaloric materials; Mn-Fe-P-Si; phase diagram; transition temperature; thermal hysteresis; magnetic entropy



Citation: You, X.; Maschek, M.; van Dijk, N.H.H.; Brück, E. Magnetic Phase Diagram of the $Mn_xFe_{2-x}P_{1-y}Si_y$ System. *Entropy* **2022**, *24*, 2. <https://doi.org/10.3390/e24010002>

Academic Editors: Luana Caron, Francesco Cugini and Xuefei Miao

Received: 10 November 2021

Accepted: 16 December 2021

Published: 21 December 2021

Publisher's Note: MDPI stays neutral with regard to jurisdictional claims in published maps and institutional affiliations.



Copyright: © 2021 by the authors. Licensee MDPI, Basel, Switzerland. This article is an open access article distributed under the terms and conditions of the Creative Commons Attribution (CC BY) license (<https://creativecommons.org/licenses/by/4.0/>).

1. Introduction

The application or removal of an external magnetic field on a magnetic solid under adiabatic conditions triggers a temperature change that is known as the magnetocaloric effect (MCE) [1]. In an isothermal process, this MCE is associated with magnetic entropy change. There are two main applications of the MCE. The first application is magnetic refrigeration, where heat is removed in a magnetic field cycle [2]. Compared to conventional gas compression refrigeration, magnetic refrigeration shows advantages, for instance, no harmful gases are released, and a high cooling efficiency can be achieved [3]. The second application is the thermomagnetic motor/generator, where waste heat is converted into mechanical/electric energy [4,5].

The key to convert current thermomagnetic motors/generators into a cost-effective application is to optimise the magnetocaloric materials. Pecharsky and Gschneidner at Ames Lab discovered a giant magnetocaloric effect in $Gd_5Si_2Ge_2$ alloys near ambient temperature [6–8]. Since then, several intermetallic material systems with a giant MCE have been discovered and developed, including La(Fe,Si)₁₃-based alloys [9–11], MnFeP(As,Ge,Si) alloys [12–16] and Ni–Mn-based Heusler alloys [17–20]. Among these magnetocaloric families, the (Mn,Fe)₂(P,Si)-type compounds have been considered as one of the most promising candidates for near-room temperature magnetic refrigeration and magnetic energy conversion applications due to their combination of a tuneable working temperature, low hysteresis, corrosion resistance, compositional stability and low material costs.

In the last decade, (Mn,Fe)₂(P,Si) compounds with varying Si-content have been thoroughly investigated for their giant MCE based on the earth-abundant and non-toxic elements [21–28]. The Mn-Fe-P-Si composition of these materials may have a distinct effect on the structural and magnetic properties. In addition, the introduction of small atoms like boron, carbon and nitrogen can also be used to tailor the magnetoelastic transition for the (Mn,Fe)₂(P,Si) compounds while preserving a giant MCE [29–32].

Dung and co-workers [33] have constructed partial phase diagrams of the (Mn,Fe)₂(P,Si) compounds and illustrated the composition dependence of the Curie temperature T_C (K)

and the thermal hysteresis ΔT_{hys} for the $\text{Mn}_x\text{Fe}_{2-x}\text{P}_{1-y}\text{Si}_y$ compounds ($x = 1.10\text{--}1.30$, $y = 0.50\text{--}0.58$). It has been found that an increase in the Mn:Fe atomic ratio causes a reduction in both T_C (K) and in thermal hysteresis ΔT_{hys} , while an increase in the P:Si atomic ratio leads to a decrease in T_C and an increase in thermal hysteresis. This study focused on a limited region of the Fe-Mn-P-Si phase diagram. A revised $\text{FeMnP}_{1-y}\text{Si}_y$ phase diagram was later presented by Höglin [34], which consists of five main zones featuring two single phase regions for the orthorhombic Co_2P -type ($y < 0.15$) structure and the hexagonal Fe_2P -type ($0.24 \leq x \leq 0.50$) structure.

In the present study, an extended phase diagram of the $\text{Mn}_x\text{Fe}_{2-x}\text{P}_{1-y}\text{Si}_y$ system is presented, with focus on the magnetocaloric active Fe_2P -phase for a wide range of compositions (for Mn fraction of $0.3 < x < 2.0$ and a Si fraction of $0.33 \leq y \leq 0.6$). This extended phase diagram enables the search of suitable compositions for magnetic refrigeration and energy conversion applications. Furthermore, the presence of impurity phase(s) and the relationship between the heat of transformation of the magnetic transition and thermal hysteresis are discussed.

2. Materials and Methods

Polycrystalline $\text{Mn}_x\text{Fe}_{2-x}\text{P}_{1-y}\text{Si}_y$ samples have been prepared by ball milling the starting materials Fe (99.9%), Mn (99.9%), red-P (99.7%) and Si (99.9%) powder. After 10 h of ball milling, the samples were pressed into tablets [14]. The tablets were sealed under Ar atmosphere in quartz ampoules, sintered at 1373 K for 25 h and then quenched into water.

Powder diffraction patterns were collected in a PANalytical X-pert Pro diffractometer with $\text{Cu } K_\alpha$ radiation. The lattice parameters and the impurity phases were obtained by a full Rietveld analysis of the X-ray diffraction data using the FULLPROF package [35]. The heat capacity and heat of transformation were measured in a differential scanning calorimeter (DSC). The measurements were carried out using a TA Q2000 DSC, which uses liquid nitrogen to cool the system. The sweeping rate was 10 K/min.

The magnetic properties were measured in a Superconducting Quantum Interface Device (SQUID) magnetometer (Quantum Design MPMS XL) using the RSO mode in the temperature range of 5–370 K with a sweep rate of 2 K/min and vibrating sample magnetometer (VSM) (Quantum Design VersaLab) in the temperature range of 300–600 K with a sweep rate of 10 K/min. From the magnetic measurements, the ferromagnetic transition temperature T_C and the thermal hysteresis ΔT_{hys} can be obtained. The values of T_C and ΔT_{hys} were determined from the maximum in the first derivative of the heating and cooling curves in an applied magnetic field of 0.01 T

3. Results

3.1. Structure

A structural analysis has been performed to refine the lattice structure of the $\text{Mn}_x\text{Fe}_{2-x}\text{P}_{1-y}\text{Si}_y$ quaternary compounds. Four possible lattice structures are found in the $\text{Mn}_x\text{Fe}_{2-x}\text{P}_{1-y}\text{Si}_y$ compounds. The orthorhombic Co_2P structure ($Pnma$) forms in the Si poor region ($y < 0.15$). The single hexagonal Fe_2P structure ($P-62m$) of Figure 1 is found for Si compositions of $0.24 \leq y \leq 0.5$. For a Si composition of $0.5 \leq y < 1.0$, a three-phase region is observed, which consists of the Fe_2P structure, the hexagonal Mn_5Si_3 structure ($P63/mcm$) and the cubic Fe_3Si structure ($Fm-3m$) [34].

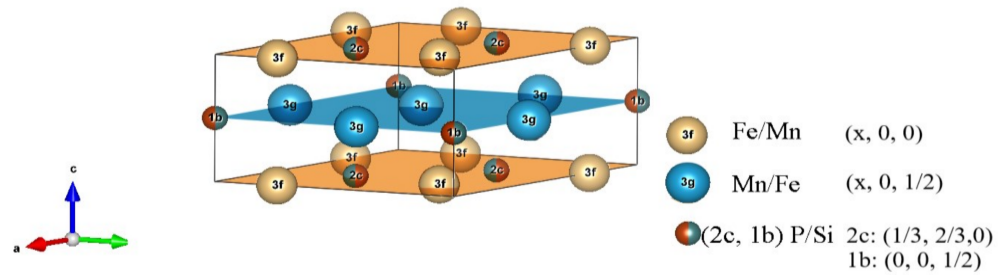


Figure 1. Unit cell of the hexagonal Fe_2P structure (space group $P-62m$) indicated is the layered structure with the Wyckoff positions. The Mn and Fe atoms occupy the $3g$ and $3f$ positions (Mn prefers the $3g$ site and Fe the $3f$ site), while the P and Si atoms occupy the $2c$ and $1b$ positions.

A silicon concentration range of $0.33 \leq y \leq 0.6$ was chosen to synthesise samples $\text{Mn}_x\text{Fe}_{2-x}\text{P}_{1-y}\text{Si}_y$ with a hexagonal Fe_2P lattice structure. The investigated range of silicon concentrations has been restricted to avoid the appearance of the orthorhombic lattice structure when the silicon concentration is too low. In contrast, if the silicon concentration is too high, the three-phase region is entered (with the Fe_2P -type main phase and Fe_3Si -type and Mn_5Si_3 -type impurity phases), resulting in a decrease in the phase fraction of the main phase [34].

In Figure 2 the evolution of the lattice parameters a and c in the hexagonal main phase of the $\text{Mn}_x\text{Fe}_{2-x}\text{P}_{1-y}\text{Si}_y$ compounds is shown as a function of composition, refined values are given in Table 1. When $x > 1$ the lattice parameter a expands for increasing Mn and Si concentrations (Figure 2a). This phenomenon can be explained in terms of the atomic radius. The manganese atom has a larger radius than the Fe atom, and Mn prefers the crystallographic $3g$ site, while Fe prefers the $3f$ site. When the $3g$ site is fully occupied, then the rest of the Mn atoms occupy the $3f$ site [30]. As a result, the lattice parameter a expands.

Table 1. Properties of compounds in the phase diagram of $\text{Mn}_x\text{Fe}_{2-x}\text{P}_{1-y}\text{Si}_y$ system.

Mn Conc. (x)	Si Conc. (y)	T _c (K)	T _{hys} (K)	Heat of Trans-Formation (J/g)	a (Å)	c (Å)	c/a	Main Phase %	Fe ₃ Si Phase %	Fe ₅ Si ₃ Phase %
0.3	0.33	362.3	0.0	2.0	5.99145(3)	3.42440(3)	0.5715	84.0 ±0.8	14.8 ±0.3	1.3 ±0.4
0.5	0.33	224.3	23.9	- ¹	5.99147(5)	3.42442(3)	0.5715	90.4 ±1.4	8.7 ±0.3	1.0 ±0.1
0.7	0.33	189.6	76.6	- ¹	5.97865(6)	3.47447(4)	0.5811	89.7 ±1.3	9.0 ±0.4	1.3 ±0.2
0.9	0.33	214.5	91.0	- ¹	5.98880(4)	3.48886(3)	0.5826	92.1 ±1.5	3.9 ±0.3	4.0 ±0.7
1.0 *	0.33	211.7	73.1	- ¹	5.99761(4)	3.48817(3)	0.5816	95.8 ±1.1	1.4 ±0.2	2.8 ±0.2
0.3	0.4	469.4	2.7	2.5	6.02914(5)	3.39681(4)	0.5634	88.2 ±1.2	11.7 ±0.4	0.1 ±0.1
0.5	0.4	324.0	2.6	2.8	6.01422(5)	3.42870(4)	0.5701	86.5 ±1.1	13.2 ±0.4	0.3 ±0.1
0.7	0.4	327.0	12.5	5.2	6.02434(5)	3.45378(3)	0.5733	93.7 ±1.1	6.3 ±0.4	0.3 ±0.1
0.9	0.4	307.1	41.2	13.3	6.02771(4)	3.47656(8)	0.5768	93.3 ±1.3	6.7 ±0.4	-
1.0	0.4	282.2	56.4	10.1	6.01853(7)	3.48194(5)	0.5785	96.0 ±1.6	3.4 ±0.3	0.6 ±0.1
1.1	0.4	219.6	54.4	- ¹	6.02441(5)	3.48591(4)	0.5786	94.4 ±1.1	4.3 ±0.2	1.3 ±0.2
1.3	0.4	146.9	26.9	- ¹	6.05270(5)	3.47604(4)	0.5743	90.3 ±1.2	0.2 ±0.0	9.5 ±0.6
1.5	0.4	73.9	0.0	- ¹	6.08221(4)	3.46432(3)	0.5696	94.7 ±1.2	1.6 ±0.4	3.7 ±0.1
1.7 *	0.4	64.9	0.0	- ¹	6.11159(5)	3.45225(3)	0.5649	86.9 ±2.4	9.2 ±2.6	3.9 ±0.2
0.5	0.5	443.3	2.7	2.0	6.06083(6)	3.40681(4)	0.5621	72.2 ±2.6	21.5 ±0.8	6.3 ±3.3
0.7	0.5	373.0	10.9	9.4	6.04712(8)	3.44757(6)	0.5701	81.3 ±1.7	18.1 ±0.7	0.6 ±0.2
0.9	0.5	362.7	29.5	16.2	6.05370(6)	3.46627(5)	0.5726	84.2 ±1.4	15.7 ±0.5	0.2 ±0.1
1.0	0.5	348.6	31.1	17.4	6.06062(4)	3.46886(3)	0.5724	87.4 ±0.9	12.2 ±3.4	0.4 ±0.1
1.3	0.5	219.1	0.0	- ¹	6.08292(5)	3.45815(4)	0.5685	89.5 ±1.5	9.2 ±0.2	1.3 ±0.2
1.5	0.5	182.7	0.3	- ¹	6.11228(3)	3.44680(3)	0.5639	88.7 ±1.0	9.2 ±0.3	2.1 ±0.1
1.7	0.5	162.5	0.0	- ¹	6.14091(5)	3.43373(4)	0.5592	83.2 ±1.1	14.4 ±0.6	2.4 ±0.2
1.9 *	0.5	142.6	2.0	- ¹	6.17221(5)	3.41687(3)	0.5536	89.3 ±1.0	10.7 ±0.7	-

Table 1. Cont.

Mn Conc. (x)	Si Conc. (y)	T _C (K)	T _{hys} (K)	Heat of Trans-Formation (J/g)	a (Å)	c (Å)	c/a	Main Phase %	Fe ₃ Si Phase %	Fe ₅ Si ₃ Phase %
0.5	0.6	473.9	0.0	0.7	6.12222(5)	3.33965(4)	0.5455	71.9 ±0.8	26.3 ±0.5	1.8 ±0.2
0.7	0.6	443.6	4.4	15.4	6.13927(5)	3.34006(4)	0.5440	79.6 ±1.0	17.8 ±0.4	2.6 ±0.2
0.9	0.6	421.9	15.4	12.0	6.09298(8)	3.43456(6)	0.5637	81.0 ±1.5	14.6 ±0.6	4.4 ±0.4
1.0	0.6	403.0	13.4	15.3	6.09631(5)	3.43886(4)	0.5641	90.6 ±1.2	8.1 ±0.4	1.3 ±0.1
1.1	0.6	364.3	15.2	8.8	6.1067(1)	3.4357(9)	0.5626	81.5 ±1.3	16.2 ±0.5	2.3 ±0.2
1.3	0.6	302.1	0.2	4.9	6.1563(1)	3.38444(9)	0.5497	79.7 ±1.3	20.1 ±0.5	0.3 ±0.1
1.5	0.6	255.2	0.0	2.0	6.14830(5)	3.41576(3)	0.5556	83.1 ±1.1	15.0 ±0.5	1.9 ±0.1
1.7	0.6	225.8	1.3	1.4	6.17386(8)	3.40240(5)	0.5511	90.8 ±1.1	4.9 ±0.0	4.4 ±0.2
1.9	0.6	191.6	0.4	- ¹	6.20058(7)	3.38632(4)	0.5461	92.1 ±1.8	2.2 ±0.3	5.7 ±0.6

¹ outside the measurement range of DSC, * at edge to unstable.

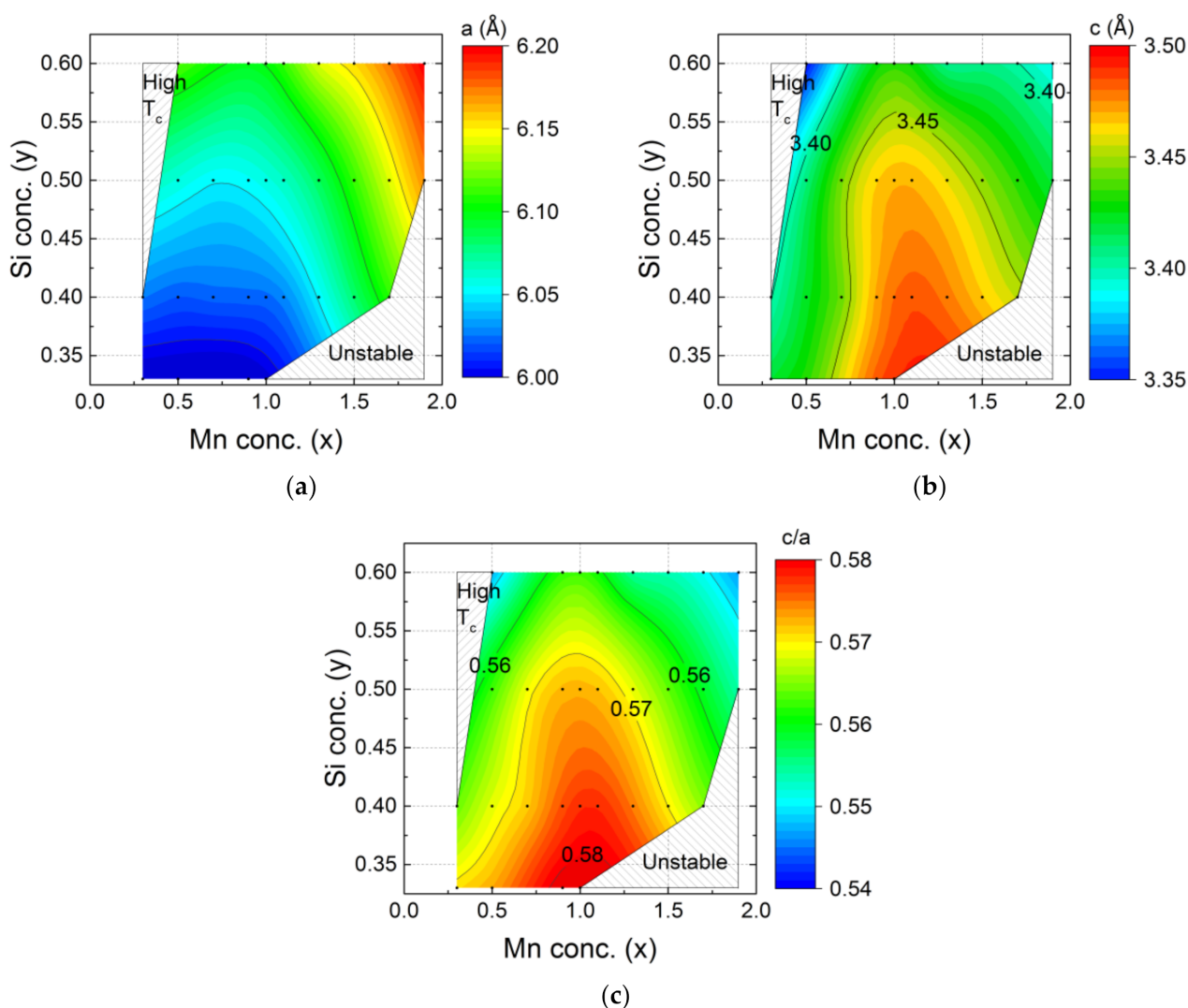


Figure 2. Composition dependence of the lattice parameters for the hexagonal Fe₂P-type main phase in the Mn_xFe_{2-x}P_{1-y}Si_y system with (a) lattice parameter *a*, (b) lattice parameter *c* and (c) the *c/a* ratio. The black points correspond to the experimental data. The colour code is obtained from linear interpolation. As the *c/a* ratio may change discontinuously at the first order ferromagnetic phase transition, all data were measured in the paramagnetic state. In Table 1.

Figure 2b indicates that the lattice parameter *c* has a maximum value when the metal ratio is Mn:Fe = 1:1 (corresponding to *x* = 1) In this case, the 3*g* site is fully occupied by

Mn and the $3f$ site is fully occupied by Fe. The lattice parameter c is found to shrink for increasing Fe, Mn or Si concentration. The c/a ratio ranges from 0.54 to 0.58 and shows a similar dependence on composition as lattice parameter c (Figure 2c).

3.2. Magnetic Properties of $Mn_xFe_{2-x}P_{1-y}Si_y$

The ferromagnetic-to-paramagnetic transition temperature T_C and the thermal hysteresis in this transition ΔT_{hys} for the hexagonal Fe_2P -type main phase in the $Mn_xFe_{2-x}P_{1-y}Si_y$ ($x = 0.3\text{--}2.0$, $y = 0.33\text{--}0.60$) compounds was investigated by magnetisation measurements and is shown in Figure 3. The ferromagnetic transition temperature T_C increases with increasing Fe and Si contents. Materials with a low thermal hysteresis ΔT_{hys} can be found for both Fe-rich and Mn-rich compositions.

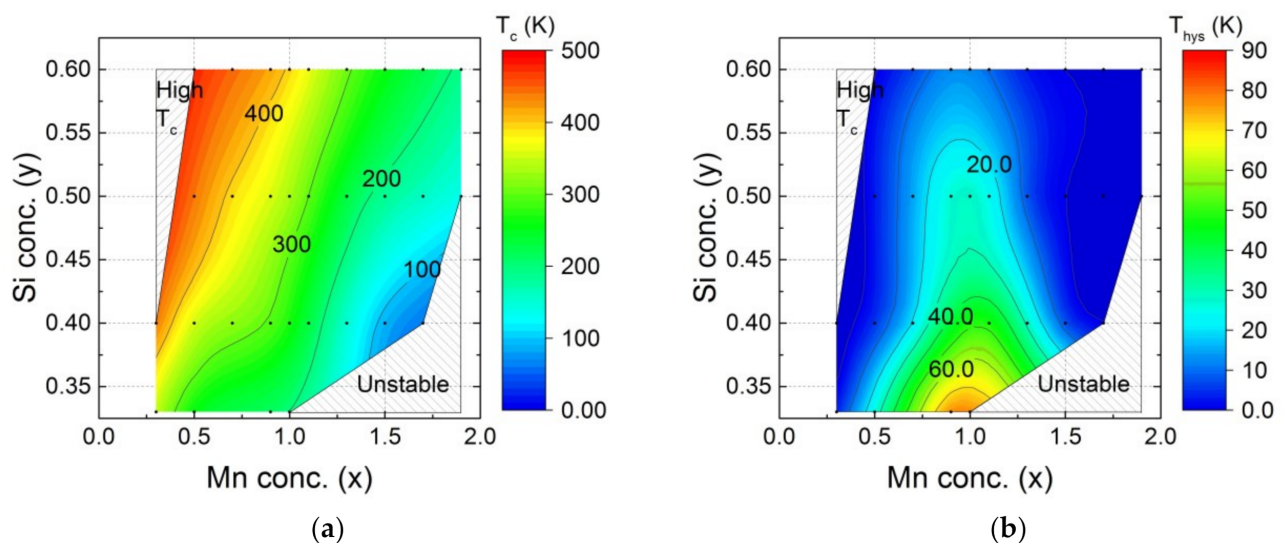


Figure 3. Magnetic properties of $Mn_xFe_{2-x}P_{1-y}Si_y$ ($x = 0\text{--}2$, $y = 0.33\text{--}0.60$) compounds showing the composition dependence of (a) the ferromagnetic transition temperature T_C and (b) the thermal hysteresis ΔT_{hys} . The black points correspond to the experimental data. The colour code is obtained from linear interpolation.

3.2.1. Transition Temperature and Thermal Hysteresis

The $Mn_xFe_{2-x}P_{1-y}Si_y$ compounds cover a broad range of ferromagnetic transition temperatures [36]. In this work, the experimental transition temperature T_C was found to range from 65 to 470 K. The highest ferromagnetic transition temperature appears in the compound $Mn_{0.3}Fe_{1.7}P_{0.6}Si_{0.4}$ ($T_C = 470$ K). This transition temperature is too high for magnetic refrigeration, magnetic heat pumping or waste heat conversion applications near room temperature. According to the trend of the phase diagram, it is clear that the transition temperature can be tuned higher if we increase the Si concentration. Therefore, part of the phase diagrams is marked 'High T_C ' as it shows a ferromagnetic transition temperature beyond the application range ($T_C > 470$ K). The compounds $Mn_{1.7}Fe_{0.3}P_{0.6}Si_{0.4}$ shows the lowest ferromagnetic transition temperature ($T_C = 65$ K) in the $Mn_xFe_{2-x}P_{1-y}Si_y$ phase diagram. In general, the highest transition temperatures are found for low Mn and high Si contents, while the lowest are found for low Fe and Si contents.

The thermal hysteresis ΔT_{hys} covers a broad range of values from 0 to 90 K. It is interesting to note that the largest hysteresis was found for a metal ratio of Fe:Mn $\approx 1:1$ ($x \approx 1$), corresponding to a full occupancy of the $3g$ site by Mn and the $3f$ site by Fe. The thermal hysteresis decreases with decreasing Fe, Mn or P content. The thermal hysteresis of the $Mn_xFe_{2-x}P_{1-y}Si_y$ compounds is further tuneable by optimising the stoichiometry [37].

3.2.2. Unstable Compositions

In Figure 3, there is an area in the compositional maps marked as ‘Unstable’. Figure 4a shows examples of the magnetisation as a function of temperature for $\text{Mn}_x\text{Fe}_{2-x}\text{P}_{1-y}\text{Si}_y$ compounds in the unstable region ($x = 1.1\text{--}1.9$, $y = 0.33$ and $x = 1.6$, $y = 0.4$). Compared to ferromagnetic Fe_2P -type samples (shown in Figure 4b), these samples generally show more than one magnetic transition, or they undergo an antiferromagnetic transition from the paramagnetic state instead of a ferromagnetic transition, while normal Fe_2P -type samples have one magnetic phase transition with a magnetisation value above $120 \text{ Am}^2/\text{kg}$ under 1 T external magnetic field. These transitions cannot be used in magnetic refrigerators nor for thermomagnetic motors. Therefore, they are not studied further.

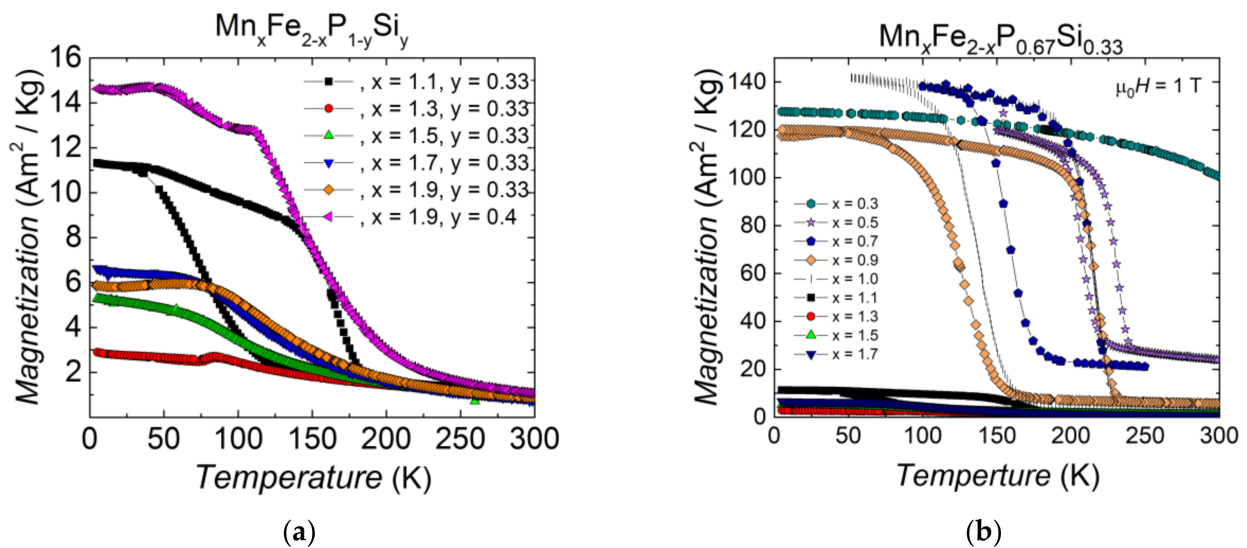


Figure 4. Magnetisation in 1 T as a function of temperature for (a) $\text{Mn}_x\text{Fe}_{2-x}\text{P}_{1-y}\text{Si}_y$ compounds in the ‘unstable’ zone and (b) Comparison of ferromagnetic and ‘unstable’ samples in $\text{Mn}_x\text{Fe}_{2-x}\text{P}_{0.67}\text{Si}_{0.33}$ compounds.

4. Discussion

4.1. Impurity Phase

The silicon concentration ($0.33 \leq y \leq 0.6$) was chosen to synthesise $\text{Mn}_x\text{Fe}_{2-x}\text{P}_{1-y}\text{Si}_y$ samples with a hexagonal Fe_2P -type lattice structure. The investigated range of silicon concentrations has been restricted to avoid the appearance of the orthorhombic lattice structure when the silicon concentration is too low. In contrast, if the silicon concentration is too high, a three-phase region is entered (consisting of the Fe_2P -type main phase and the Fe_3Si -type and Mn_5Si_3 -type impurity phases), resulting in a decrease in the phase fraction of the main phase [34]. The phase stability diagrams for the phase composition of the Fe_2P -type main phase and the Fe_3Si -type [27] and Mn_5Si_3 -type impurity phases are shown in Figure 5. The main impurity phase in the iron-rich $\text{Mn}_x\text{Fe}_{2-x}\text{P}_{1-y}\text{Si}_y$ compounds ($x < 1$) is the Fe_3Si -type phase. Figure 5b indicates that the Fe_3Si -type impurity increases continuously for increasing Fe and Si concentrations. For high Mn and low Si concentrations, the Mn_5Si_3 -type impurity phase is dominant (Figure 5c).

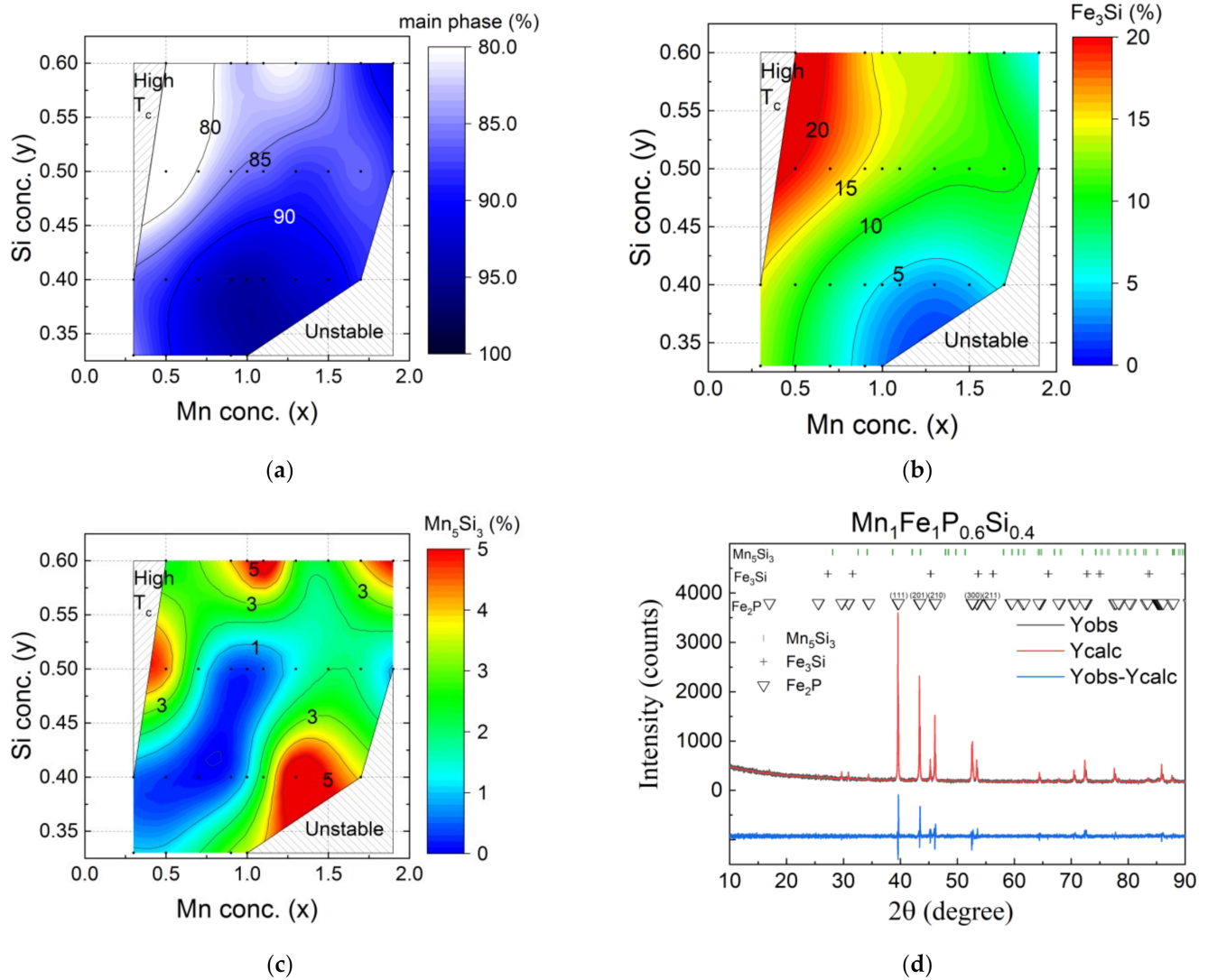


Figure 5. Phase stability diagrams of the $\text{Mn}_x\text{Fe}_{2-x}\text{P}_{1-y}\text{Si}_y$ ($x = 0.3\text{--}2.0$ and $y = 0.33\text{--}0.60$) system showing the phase fractions of (a) the Fe₂P-type main phase, (b) the Fe₃P-type impurity phase and (c) the Mn₅Si₃-type impurity phase. The black points correspond to the experimental data. The colour code is obtained from linear interpolation. (d) XRD pattern of MnFeP_{0.6}Si_{0.4} with measured and calculated intensities.

By optimising the stoichiometry, the transition temperature T_C and the thermal hysteresis ΔT_{hys} can change significantly. As shown in Figure 6, in Mn_{0.7}Fe_{1.3-z}P_{0.6}Si_{0.4} a change in the Fe content from 1.30 ($z = 0.00$) to 1.21 ($z = 0.09$) results in an increase in transition temperature of 52 K and a decrease in thermal hysteresis of 10 K. These changes are caused by a variation in the amount of impurity phase and a shift in Mn, Fe ratio and P, Si ratio [12]. From the X-ray refinement, the nominally stoichiometric sample Mn_{0.7}Fe_{1.3}P_{0.6}Si_{0.4} has about 6% Fe₃Si impurity. (Figure 6b) The impurity phase can be removed by optimising the stoichiometry, which is accompanied by an increase in T_C . Considering this behaviour, it is better to start the material synthesis with a T_C below the desired working temperature and then adjust it by reducing impurities.

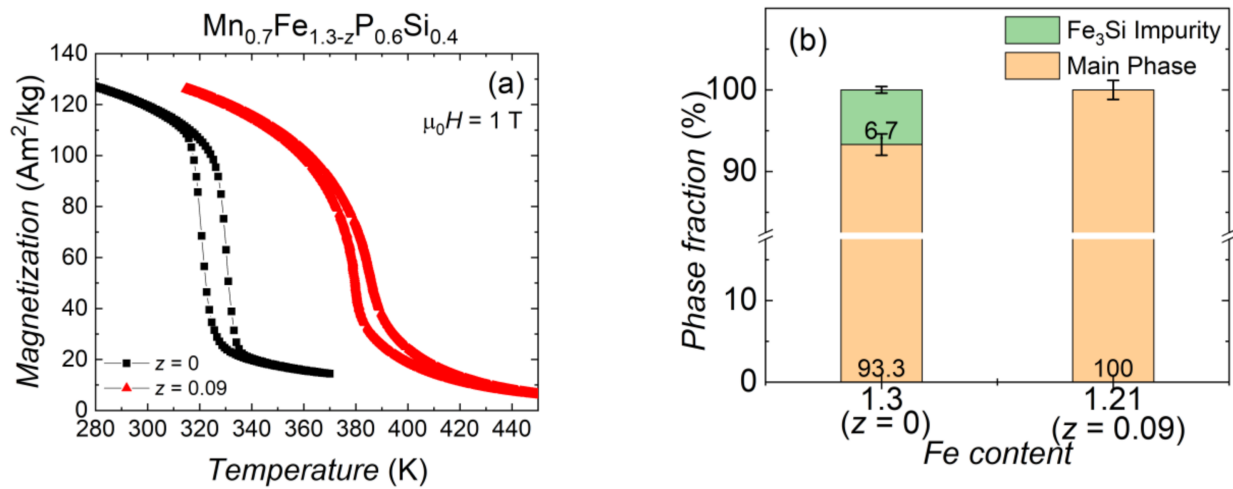


Figure 6. (a) Magnetisation as a function of temperature for $\text{Mn}_{0.7}\text{Fe}_{1.3-z}\text{P}_{0.6}\text{Si}_{0.4}$ for $z = 0.00$ and 0.09 sample, measured in an applied magnetic field of 1 T. (b) The phase fraction of the $\text{Mn}_{0.7}\text{Fe}_{1.3-z}\text{P}_{0.6}\text{Si}_{0.4}$ for $z = 0.00$ and 0.09 sample obtained from X-ray diffraction.

4.2. Heat of Transformation and Thermal Hysteresis as a Function of Structural Parameters

The heat of transformation of the magnetic phase transition and thermal hysteresis are two intuitive indicators that can reveal the usability of a material for magnetocaloric applications. Often, a first order magnetic phase transition (FOMT) is associated with a large heat of transformation and a large hysteresis. For applications we like to have large magnetic entropy changes that can be boosted by contributions from heat of transformation, at the same time thermal hysteresis exceeding the adiabatic temperature change can't be utilized in simple magnetisation and demagnetisation cycles. Therefore, these two parameters as important characteristics are compared to c/a ratio in this work.

Figure 7a shows the temperature dependence of the specific heat and large entropy change at the magnetic phase transition of samples $\text{Mn}_{1.3}\text{Fe}_{0.7}\text{P}_{0.5}\text{Si}_{0.5}$ and $\text{Mn}_{1.3}\text{Fe}_{0.7}\text{P}_{0.4}\text{Si}_{0.6}$. These two samples both show a relatively large sharp peak, and the heat of magnetic transformation ΔQ_m can be obtained by integrating the peak area. Note that this specific-heat peak contains all thermal effects involved in the magnetic phase transition. The ΔQ_m of $\text{Mn}_{1.3}\text{Fe}_{0.7}\text{P}_{0.5}\text{Si}_{0.5}$ and $\text{Mn}_{1.3}\text{Fe}_{0.7}\text{P}_{0.4}\text{Si}_{0.6}$ compounds is 4.72 and 4.58 (J g^{-1}), respectively.

A clear correlation becomes visible when the thermal hysteresis is compared to the c/a ratio of the lattice parameters for the Fe_2P -type hexagonal main phase of the $\text{Mn}_x\text{Fe}_{2-x}\text{P}_{1-y}\text{Si}_y$ system observed. As shown in Figure 7b, the lowest c/a ratio starts from 0.5455 ($\text{Mn}_{0.5}\text{Fe}_{1.5}\text{P}_{0.4}\text{Si}_{0.6}$) and ends at 0.5826 ($\text{Mn}_{0.9}\text{Fe}_{1.1}\text{P}_{0.67}\text{Si}_{0.33}$). Most samples display no hysteresis when the c/a ratio is smaller than 0.57. For instance, sample $\text{Mn}_{1.5}\text{Fe}_{0.5}\text{P}_{0.6}\text{Si}_{0.4}$ is a sample without thermal hysteresis ($c/a = 0.5696$) and sample $\text{Mn}_{0.5}\text{Fe}_{1.5}\text{P}_{0.6}\text{Si}_{0.4}$ is a sample with a 2.6 K thermal hysteresis ($c/a = 0.5701$). In the grey region $0.56 < c/a < 0.57$ we find both samples with and without hysteresis, and when the c/a ratio is larger than 0.57 a steep increase in hysteresis with increasing c/a ratio. For instance, sample $\text{Mn}_{0.7}\text{Fe}_{1.3}\text{P}_{0.5}\text{Si}_{0.5}$ is a FOMT sample with about 12 K thermal hysteresis ($c/a = 0.5701$). The red line is a linear fit to these data.

In Figure 7c the heat of magnetic transformation is compared to the c/a ratio of the lattice parameters (Figure 2c) for the Fe_2P -type hexagonal main phase for the $\text{Mn}_x\text{Fe}_{2-x}\text{P}_{1-y}\text{Si}_y$ system. There is no clear trend that these two parameters are related.

In general, thermal hysteresis is controlled by the phase nucleation, which is a kinetic process, and the c/a ratio is a parameter of the crystal structure. The reason why these two parameters correlated is not directly obvious. It could be that the hysteresis is related to the unit-cell distortion when the transition is crossed. This interesting experimental relationship between thermal hysteresis and the c/a ratio deserves further study.

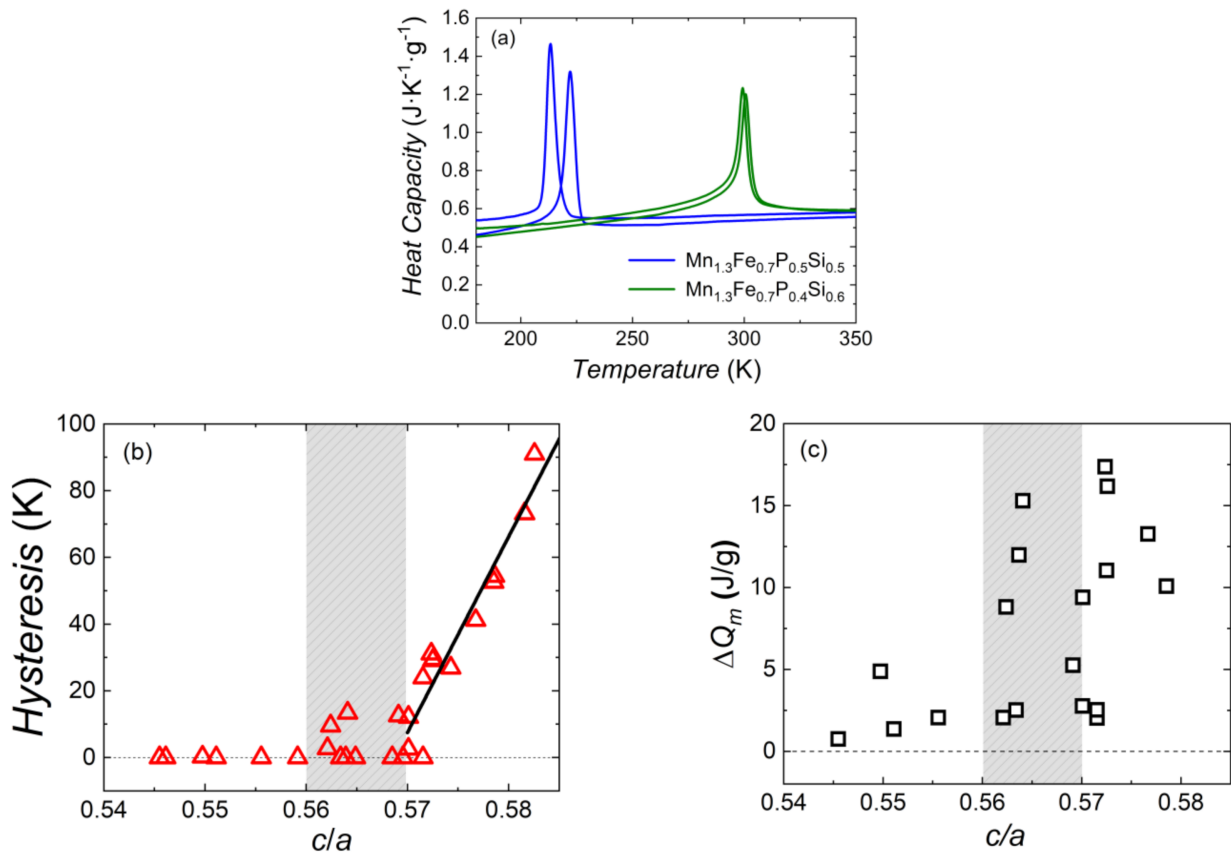


Figure 7. (a) Temperature dependence of the specific heat of sample Mn_{1.3}Fe_{0.7}P_{0.5}Si_{0.5} and Mn_{1.3}Fe_{0.7}P_{0.4}Si_{0.6} measured in zero fields upon cooling and heating. Thermal hysteresis (b) and heat of magnetic transformation ΔQ_m (c) as a function of the c/a ratio for the lattice parameters of the hexagonal Fe₂P-type main phase of the Mn_{*x*}Fe_{2-*x*}P_{1-*y*}Si_{*y*} system.

4.3. Suitable Materials for Magnetic Energy Conversion Applications

The structural, magnetic and phase stability diagrams allow us to identify proper candidates for each application in different working temperature range. Based on this working temperature window, contour lines can be drawn in the magnetic diagram for T_C (Figure 8b) and duplicate them at the same positions in the diagram for the thermal hysteresis (Figure 8c). The obtained information on the transition temperature and thermal hysteresis is summarised in Figure 8a. In Figure 8a, the x, y axis represents the Mn and Si concentration, respectively, The z axis represents thermal hysteresis obtained from the thermal contour line drawn in the thermal hysteresis part of the phase diagram (Figure 8c). These 3D concentration dependence of the thermal hysteresis graph has projections on the xy plane, which are the same as the contour lines shown in the phase diagram.

As an example for the working temperature range of a thermomagnetic motor being between 20 °C (293 K) and 60 °C (333 K), with an optimal T_C of 40 °C (313 K). For each temperature, the hysteresis increases with increasing Mn and Si concentration. Then, the hysteresis drops after it reaches a peak for a Mn content of $x \approx 1.0$ and a Si content of $y \approx 0.45$. Promising candidates can only be found in the grey area in Figure 8a, which correspond to the Fe-rich/P-rich part ($x < 0.7, y < 0.4$) and the Mn-rich/Si-rich part ($x > 1.1, y > 0.5$) of the phase diagram.

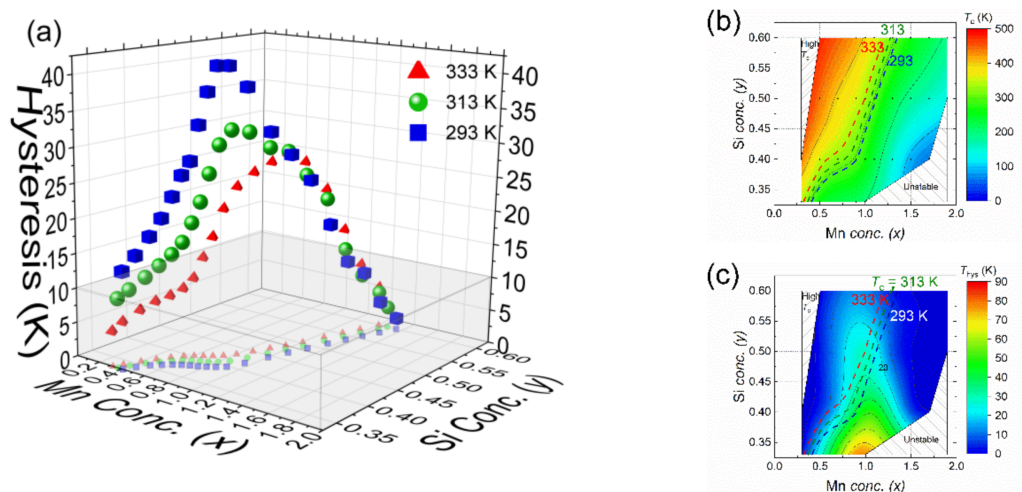


Figure 8. (a) Concentration dependence of the thermal hysteresis in the $Mn_xFe_{2-x}P_{1-y}Si_y$ system for transition temperatures T_C of 293, 313 and 333 K. The points correspond to interpolated values in the magnetic diagram. The blue and red symbols and lines mark the lower and upper temperature limit of the optimal cycling range between 20 °C (293 K) and 60 °C (333 K). The green symbols and line mark the considered optimal T_C of 40 °C (313 K). Schematic graph with contour lines in phase diagram of $Mn_xFe_{2-x}P_{1-y}Si_y$ ($x = 0-2$, $y = 0.33-0.60$) compounds showing the composition dependence of (b) the ferromagnetic transition temperature T_C and (c) the thermal hysteresis ΔT_{hys} .

5. Conclusions

A full-range magnetic phase diagram of the $Mn_xFe_{2-x}P_{1-y}Si_y$ system has been established as a guide to find suitable materials for energy conversion applications in a thermomagnetic motor. We find a strong correlation between thermal hysteresis and c/a ratio, however, there are a wide range of samples with low (<2 K) or absent hysteresis that yet display large heat of magnetic transformation. Both Mn-rich with a high Si and Fe-rich samples with a low Si concentration were found to show a low hysteresis that can form promising candidates for applications in a thermomagnetic motor. It appears that Mn-rich samples are most suited for applications well below room temperature, while Mn-poor samples can be utilised at higher temperatures. The interesting experimental relationship between thermal hysteresis and the c/a ratio deserves further study. Furthermore, reducing the impurity phase fraction by optimising stoichiometry is important in lowering thermal hysteresis.

Author Contributions: X.Y.: investigation, writing—original draft preparation; M.M.: supervision; N.H.H.v.D. and E.B.: writing—review and editing, supervision, funding acquisition. All authors have read and agreed to the published version of the manuscript.

Funding: This research was funded by the Dutch Technology Foundation STW, which is part of the Netherlands Organisation for Scientific Research (NWO), and which is partly funded by the Ministry of Economic Affairs (OTP project 14013). M. Maschek received financial support from the EIT Climate KIC project “Local, magnetocaloric power conversion opportunities for Cities” (ID 210045).

Data Availability Statement: The data are available upon reasonable request.

Acknowledgments: The authors thank Anton Lefering and Bert Zwart for the technical support.

Conflicts of Interest: The authors declare no conflict of interest.

References

1. Cyrot, M.; Décorps, M.; Diény, B.; de Lacheisserie, E.d.T.; Néel, L.L.; Geoffroy, O. *Magnetism, Materials and Applications*; Lacheisserie, É.d.T.d., Gignoux, D., Schlenker, M., Eds.; Springer: Berlin/Heidelberg, Germany, 2005; p. 542.
2. Pecharsky, V.K.; Gschneidner, K.A. Magnetocaloric effect and magnetic refrigeration. *J. Magn. Magn. Mater.* **1999**, *200*, 44–56. [[CrossRef](#)]

3. Phan, M.-H.; Yu, S.-C. Review of the magnetocaloric effect in manganite materials. *J. Magn. Magn. Mater.* **2007**, *308*, 325–340. [[CrossRef](#)]
4. Kirol, L.D.; Mills, J.I. Numerical analysis of thermomagnetic generators. *J. Appl. Phys.* **1984**, *56*, 824–828. [[CrossRef](#)]
5. Zhan, G.-D.; Kuntz, J.D.; Mukherjee, A.K.; Zhu, P.; Koumoto, K.J.S.M. Thermoelectric properties of carbon nanotube/ceramic nanocomposites. *Scr. Mater.* **2006**, *54*, 77–82. [[CrossRef](#)]
6. Pecharsky, V.K.; Gschneidner, K.A. Giant magnetocaloric effect in Gd-5(Si₂Ge₂). *Phys. Rev. Lett* **1997**, *78*, 4494–4497. [[CrossRef](#)]
7. Pecharsky, V.K.; Gschneidner, K.A. Tunable magnetic regenerator alloys with a giant magnetocaloric effect for magnetic refrigeration from similar to 20 to similar to 290 K. *Appl. Phys. Lett.* **1997**, *70*, 3299–3301. [[CrossRef](#)]
8. Aksoy, S.; Yucel, A.; Elerman, Y.; Krenke, T.; Acet, M.; Moya, X.; Manosa, L. The influence of gallium on the magnetocaloric properties of Gd₅Si₂Ge₂. *J. Alloys Compd.* **2008**, *460*, 94–98. [[CrossRef](#)]
9. Hu, F.; Shen, B.-g.; Sun, J.-r.; Cheng, Z.-h.; Rao, G.-h.; Zhang, X.-x. Influence of negative lattice expansion and metamagnetic transition on magnetic entropy change in the compound LaFe_{11.4}Si_{1.6}. *Appl. Phys. Lett.* **2001**, *78*, 3675–3677. [[CrossRef](#)]
10. Fujieda, S.; Fujita, A.; Fukamichi, K. Large magnetocaloric effect in La (Fe_xSi_{1-x})₁₃ itinerant-electron metamagnetic compounds. *Appl. Phys. Lett.* **2002**, *81*, 1276–1278. [[CrossRef](#)]
11. Hu, F.X.; Shen, B.G.; Sun, J.R.; Wang, G.J.; Cheng, Z.H. Very large magnetic entropy change near room temperature in LaFe_{11.2}Co_{0.7}Si_{1.1}. *Appl. Phys. Lett.* **2002**, *80*, 826–828. [[CrossRef](#)]
12. Tegus, O.; Bruck, E.; Buschow, K.H.J.; de Boer, F.R. Transition-metal-based magnetic refrigerants for room-temperature applications. *Nature* **2002**, *415*, 150–152. [[CrossRef](#)] [[PubMed](#)]
13. Trung, N.T.; Ou, Z.Q.; Gortenmulder, T.J.; Tegus, O.; Buschow, K.H.J.; Bruck, E. Tunable thermal hysteresis in MnFe(P,Ge) compounds. *Appl. Phys. Lett.* **2009**, *94*, 102513. [[CrossRef](#)]
14. Dung, N.H.; Zhang, L.; Ou, Z.Q.; Brück, E. From first-order magneto-elastic to magneto-structural transition in (Mn,Fe)_{1.95}P_{0.50}Si_{0.50} compounds. *Appl. Phys. Lett.* **2011**, *99*, 092511. [[CrossRef](#)]
15. Yibole, H.; Guillou, F.; Zhang, L.; Van Dijk, N.; Brück, E.J.J.o.P.D.A.P. Direct measurement of the magnetocaloric effect in MnFe (P, X)(X= As, Ge, Si) materials. *J. Phys. D Appl. Phys.* **2014**, *47*, 075002. [[CrossRef](#)]
16. Tegus, O.; Fuquan, B.; Dagula, W.; Zhang, L.; Brück, E.; Si, P.Z.; Boer, F.R.; Buschow, K.H.J. Magnetic-entropy change in Mn_{1.1}Fe_{0.9}P_{0.7}As_{0.3-x}Ge_x. *J. Alloy. Compd.* **2005**, *396*, 6–9. [[CrossRef](#)]
17. Krenke, T.; Acet, M.; Wassermann, E.F.; Moya, X.; Mañosa, L.; Planes, A. Martensitic transitions and the nature of ferromagnetism in the austenitic and martensitic states of Ni–Mn–Sn alloys. *Phys. Rev. B* **2005**, *72*. [[CrossRef](#)]
18. Liu, J.; You, X.; Huang, B.; Batashev, I.; Maschek, M.; Gong, Y.; Miao, X.; Xu, F.; van Dijk, N.; Brück, E. Reversible low-field magnetocaloric effect in Ni–Mn–In-based Heusler alloys. *Phys. Rev. Mater.* **2019**, *3*, 084409. [[CrossRef](#)]
19. Wang, W.; Li, H.; Ren, J.; Fu, J.; Zhai, Q.; Luo, Z.; Zheng, H. Enhanced magnetocaloric properties in annealed Heusler Ni–Mn–Sn ribbons. *J. Magn. Magn. Mater.* **2015**, *374*, 153–156. [[CrossRef](#)]
20. Trombi, L.; Cugini, F.; Rosa, R.; Amadè, N.S.; Chicco, S.; Solzi, M.; Veronesi, P. Rapid microwave synthesis of magnetocaloric Ni–Mn–Sn Heusler compounds. *Scr. Mater.* **2020**, *176*, 63–66. [[CrossRef](#)]
21. Thanh, D.T.C.; Brueck, E.; Trung, N.T.; Klaasse, J.C.P.; Buschow, K.H.J.; Ou, Z.Q.; Tegus, O.; Caron, L. Structure, magnetism, and magnetocaloric properties of MnFeP_{1-x}Si_x compounds. *J. Appl. Phys.* **2008**, *103*, 07B318. [[CrossRef](#)]
22. Katagiri, K.; Nakamura, K.; Wada, H. Magnetocaloric properties and magnetic refrigerant capacity of MnFeP_{1-x}Si_x. *J. Alloy. Compd.* **2013**, *553*, 286–290. [[CrossRef](#)]
23. Höglin, V.; Hudl, M.; Sahlberg, M.; Nordblad, P.; Beran, P.; Andersson, Y. The crystal and magnetic structure of the magnetocaloric compound FeMnP_{0.5}Si_{0.5}. *J. Solid State Chem.* **2011**, *184*, 2434–2438. [[CrossRef](#)]
24. Hudl, M.; Häggström, L.; Delczeg-Czirjak, E.-K.; Höglin, V.; Sahlberg, M.; Vitos, L.; Eriksson, O.; Nordblad, P.; Andersson, Y. Strongly enhanced magnetic moments in ferromagnetic FeMnP_{0.5}Si_{0.5}. *Appl. Phys. Lett.* **2011**, *99*, 152502. [[CrossRef](#)]
25. Lai, J.; You, X.; Dugulan, I.; Huang, B.; Liu, J.; Maschek, M.; van Eijck, L.; van Dijk, N.; Brück, E. Tuning the magneto-elastic transition of (Mn,Fe,V)₂(P,Si) alloys to low magnetic field applications. *J. Alloys Compd.* **2020**, *821*, 153451. [[CrossRef](#)]
26. Lai, J.; Huang, B.; Miao, X.; Van Thang, N.; You, X.; Maschek, M.; van Eijck, L.; Zeng, D.; van Dijk, N.; Brück, E. Combined effect of annealing temperature and vanadium substitution for magnetocaloric Mn_{1.2-x}V_xFe_{0.75}P_{0.5}Si_{0.5} alloys. *J. Alloys Compd.* **2019**, *803*, 671–677. [[CrossRef](#)]
27. Maschek, M.; You, X.; Boeije, M.F.J.; Chernyshov, D.; van Dijk, N.H.; Brück, E. Charge redistribution and the magnetoelastic transition across the first-order magnetic transition in (Mn,Fe)₂(P,Si,B). *Phys. Rev. B* **2018**, *98*. [[CrossRef](#)]
28. Guillou, F.; Porcari, G.; Yibole, H.; van Dijk, N.; Bruck, E. Taming the First-Order Transition in Giant Magnetocaloric Materials. *Adv. Mater.* **2014**, *26*, 2671–2675. [[CrossRef](#)] [[PubMed](#)]
29. Guillou, F.; Yibole, H.; Porcari, G.; Zhang, L.; van Dijk, N.H.; Brück, E. Magnetocaloric effect, cyclability and coefficient of refrigerant performance in the MnFe(P, Si, B) system. *J. Appl. Phys.* **2014**, *116*, 063903. [[CrossRef](#)]
30. Miao, X.F.; Thang, N.V.; Caron, L.; Yibole, H.; Smith, R.L.; van Dijk, N.H.; Brück, E. Tuning the magnetoelastic transition in (Mn,Fe)₂(P,Si) by B, C, and N doping. *Scr. Mater.* **2016**, *124*, 129–132. [[CrossRef](#)]
31. Thang, N.V.; Miao, X.F.; van Dijk, N.H.; Brück, E. Structural and magnetocaloric properties of (Mn,Fe)₂(P,Si) materials with added nitrogen. *J. Alloys Compd.* **2016**, *670*, 123–127. [[CrossRef](#)]
32. Thang, N.; Yibole, H.; Miao, X.; Goubitz, K.; Van Eijck, L.; Van Dijk, N.; Brück, E.J.J. Effect of Carbon Doping on the Structure and Magnetic Phase Transition in (Mn, Fe)₂(P, Si). *JOM* **2017**, *69*, 1432–1438. [[CrossRef](#)]

33. Dung, N.H.; Ou, Z.Q.; Caron, L.; Zhang, L.; Thanh, D.T.C.; de Wijs, G.A.; de Groot, R.A.; Buschow, K.H.J.; Brück, E. Mixed Magnetism for Refrigeration and Energy Conversion. *Adv. Energy Mater.* **2011**, *1*, 1215–1219. [[CrossRef](#)]
34. Höglin, V.; Cedervall, J.; Andersson, M.S.; Sarkar, T.; Hudl, M.; Nordblad, P.; Andersson, Y.; Sahlberg, M. Phase diagram, structures and magnetism of the FeMnP_{1-x}Si_x system. *RSC Adv.* **2015**, *5*, 8278–8284. [[CrossRef](#)]
35. Rodriguez-Carvajal, J. *Abstract Satellite Meeting on Powder Diffraction*; Congr. Int. Union of Crystallography: Toulouse, France, 1990.
36. Brück, E.; Tegus, O.; Cam Thanh, D.T.; Trung, N.T.; Buschow, K.H.J. A review on Mn based materials for magnetic refrigeration: Structure and properties. *Int. J. Refrig.* **2008**, *31*, 763–770. [[CrossRef](#)]
37. Leif, L.; Gulzar, T.; Olof, B.; Bertil, C.; Stig, R. First Order Magnetic Phase Transition in Fe₂P. *Phys. Scr.* **1978**, *17*, 39.